# Graphene Photonics I/Q Modulator for Advanced Modulation Formats

Vito Sorianello,* Alberto Montanaro, Marco Angelo Giambra, Nadia Ligato, Wolfgang Templ, Paola Galli, and Marco Romagnoli

ACCESS | 📊 Metrics & More | 📖 Article Recommendations | 🄪 Supporting Information

**ABSTRACT:** Starting from its classical domain of long distance links, optical communication is conquering new application areas down to chip-to-chip interconnections in response to the ever-increasing demand for higher bandwidth. The use of coherent modulation formats, typically employed in long-haul systems, is now debated to be extended to short links to increase the bandwidth density. Next-generation transceivers are targeting high bandwidth, high energy efficiency, compact footprint, and low cost. Integrated photonics is the only technology to reach this goal, and silicon photonics is expected to play the leading actor. However, silicon modulators have some limits, in terms of bandwidth and footprint. Graphene is an ideal material to be integrated with silicon photonics to meet the requirements of next generation transceivers. This material provides optimal properties: high mobility, fast carrier dynamics and ultrabroadband optical properties. Graphene photonics for direct detection systems based on binary modulation formats have been demonstrated so far, including electro-absorption modulators, phase modulators, and photodetectors. However, coherent modulation for increased data-rates has not yet been reported for graphene photonics yet. In this work, we present the first graphene photonics I/Q modulator based on four graphene on silicon electro-absorption modulators for advanced modulation formats and demonstrate quadrature phase shift keying (QPSK) modulation up to 40 Gb/s.

**KEYWORDS:** coherent modulation, graphene photonics, I/Q modulator, silicon photonics
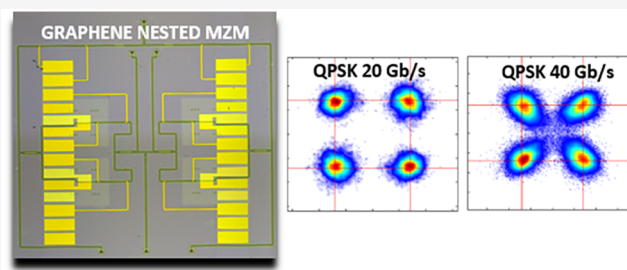
## INTRODUCTION

Graphene integrated photonics is an emerging technology[1,2] with disruptive potential arising from the combination of peculiar material properties[3,4] of graphene, i.e., the most famous bidimensional (2D) material. Graphene attracted the interest of the photonic research community because of four main features: zero-bandgap for operation (detection and modulation) over an extremely broad spectrum of wavelengths (from visible to far-infrared);[5] efficient tunability of the chemical potential by a field-effect that permits optical absorption and refraction modulation, i.e., amplitude and phase modulation of light;[6] ultrahigh carriers' mobility, exceeding $100000$ $cm^2V^{-1}s^{-1}$ in high quality samples[7,8] enabling hundreds of GHz operation[9,10] ease of integration on passive integrated photonic platforms as for instance SOI or SiN.[11,12] These properties are in their combination very appealing for many photonic applications, from sensing[13−15] to datacom/telecom.[1] Since the first demonstrations of graphene on integrated photonic waveguides for amplitude modulators[16,17] and detectors,[18] a lot of effort has been dedicated to the development of reliable technology processes toward the wafer scale integration of high mobility graphene on integrated photonic platforms.[11,12] At the chip level, many devices with improved performance have been demonstrated so far: phase

modulators (PMs) up to 10Gb/s based on a single layer of graphene (SLG) on doped silicon (Si) waveguide;[19] electro-absorption modulators (EAMs) featuring up to 50 Gb/s on−off keying (OOK)[20] and 40 GHz electro-optical bandwidth[21] based on two SLG on passive Si waveguide; SLG on Si waveguide photodetectors based on both the bolometric effect and photothermoelectric effect for detection of $\geq100$ Gb/s.[22]

Graphene modulators have been used for simple OOK amplitude modulation so far.[23] However, optical communications often require encoding the information on coherent modulation schemes, e.g., quadrature phase-shift keying (QPSK) or quadrature amplitude modulation (QAM), to enhance the spectral efficiency and increase the data transmission capacity.[24] Coherent optics is typically used in telecom applications for long-haul transmissions.[25] However, the ever-increasing demand for exchange and management of
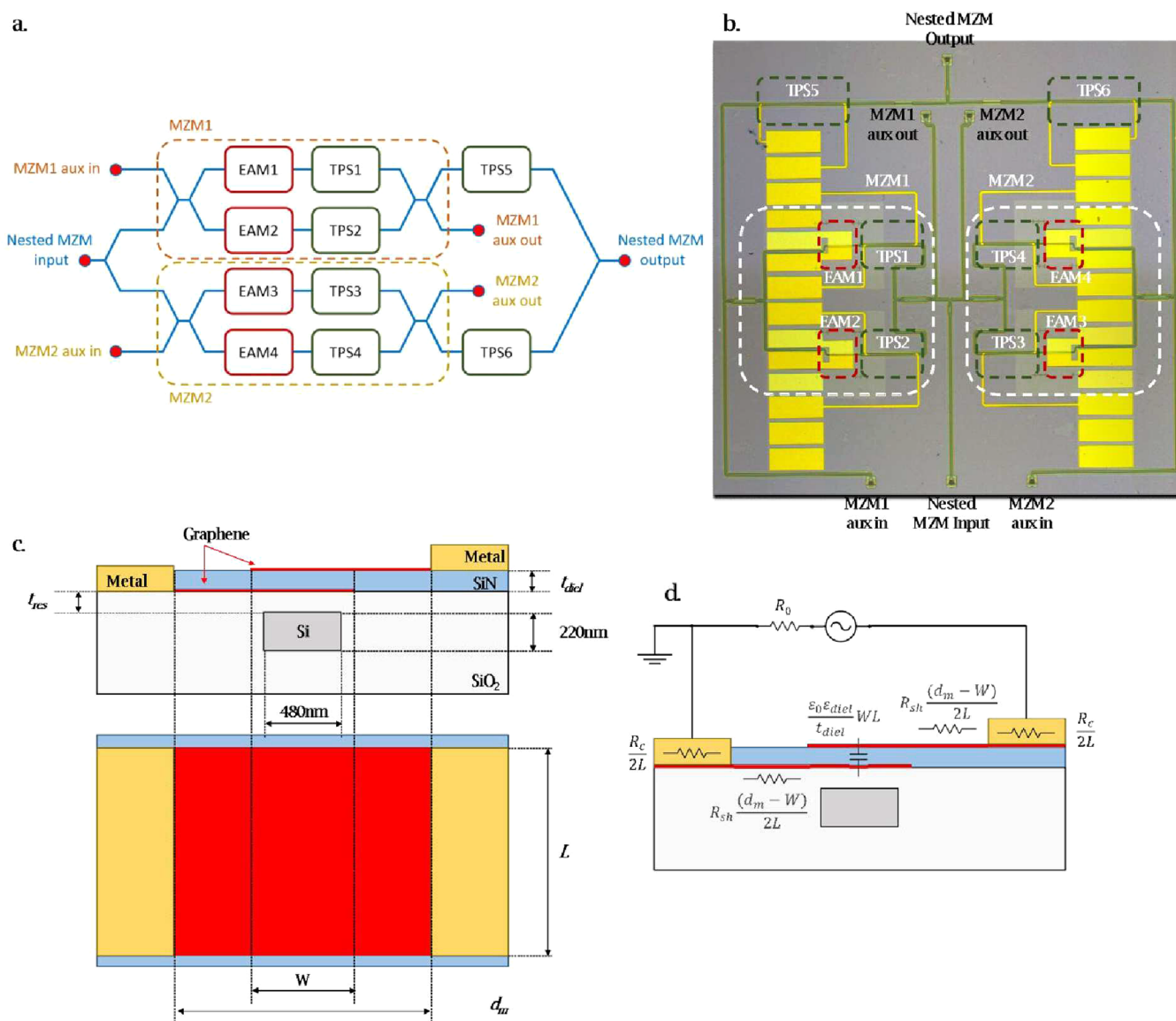
**Figure 1.** (a) Schematic layout of the designed I/Q modulator. (b) Optical microscope image of the fabricated device. (c) Double SLG EAM cross-section and top view geometry. (d) Equivalent RC circuit of the double SLG EAMs.

huge amounts of data includes coherent optics for data communications inter and intra datacenters.[26−28]

Coherent modulators for QPSK or QAM signals consist of at least two (typically four, two couples in push−pull configuration) high speed modulators combined together within a nested Mach−Zehnder interferometer (MZI), resulting in the so-called In-phase and Quadrature (I/Q) Mach−Zehnder modulator (MZM).[24] Bulk lithium niobate (LN) nested MZI based on high-speed PMs have been successfully used for decades at the transmitter side in long-haul links.[29] These devices are very fast[29,30] but typically bulky (several cm scale), which poses a limit to their use in future systems where a high level of integration and miniaturization will be required. Integrated photonics technology made available modern I/Q modulators with a high level of integration.[31] Si photonics,[32] III−V[33] and recently thin film LN[34] and plasmonic-organic hybrid (POH)[35] platforms have been used to demonstrate high performance I/Q MZM, with Si photonics and III−V solutions already available on the market. However, these technologies have potential limits:

III−V integrated photonics provides very fast and efficient solutions but at the cost of a very expensive technology because of the relatively poor yield of manufacturing and small wafer size; Si photonics provides probably the best solution for high-yield photonic integrated circuits (PICs). However Si MZM modulators based on the free carrier effect are typically long devices in the millimeter scale and feature a foreseen bandwidth limit of merely 35 GHz for standard SOI technology,[36] although a record bandwidth of 60 GHz has been demonstrated with more sophisticated technology involving Si substrate removal;[37] thin film LN provides very high speed and efficiency, but a lower level of integration (several millimeter or even centimeter scale) and higher cost;[38] despite the impressive results in terms of bandwidth (modulators with several hundreds of GHz bandwidth[39]) POH suffers high losses and low yield. Recently, a novel design based on silicon germanium (SiGe) EAMs integrated in a nested MZM has been proposed for carrier-less QPSK and 16QAM generation.[40] Taking advantage of the compact footprint (40 μm length), the SiGe EAMs exhibit 67 GHz
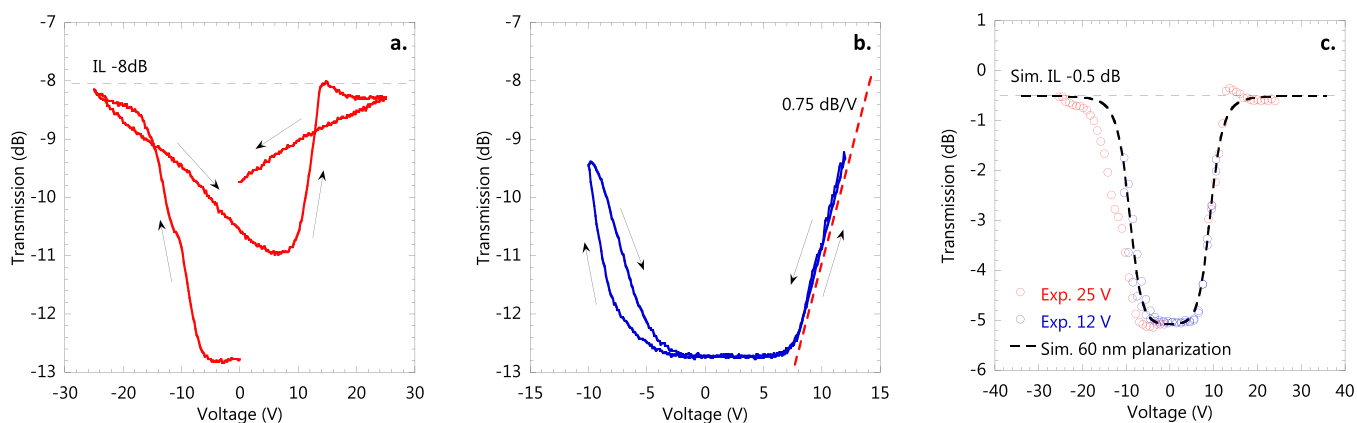
**Figure 2.** (a) EAM optical transmission vs applied voltage in the range −25 to 25 V. The transmission is normalized to the passive waveguide IL. (b) EAM optical transmission versus applied voltage in the range of −10 to 12 V. The transmission is normalized to the passive waveguide IL. (c) Numerical fit of the curves in panel a (red dots) and panel b (blue dots) with the simulated optical transmission of a double SLG EAM with 60 nm of SiO$_2$ planarized cladding on top of the waveguide (black dashed line).

bandwidth permitting demonstration of QPSK modulation at 100 Gbaud and QAM at 50 GBaud.[40] SiGe EAMs are monolithic Si photonic devices based on the Franz−Keldysh effect,[41] providing a small footprint and high speed. However, the operation wavelength range is intrinsically limited by the Ge content in the SiGe alloy, e.g., these devices are not suitable for operation in the O-Band and the operating point is temperature sensitive.

In this scenario, graphene photonics may play its part with very fast, compact, energy-efficient, wide wavelength range (being a gapless material), and cheaper solutions.[1] While an integrated photonic coherent receiver based on graphene photodetectors has been recently demonstrated,[42] the demonstration of a coherent transmitter is still missing. In this work, we report for the first time QPSK modulation up to 40 Gb/s using a nested MZM equipped with four double SLG graphene-on-Si-waveguides EAMs.

## ■ DEVICE DESIGN AND FABRICATION

The I/Q modulator layout and optical microscope image of the fabricated device are shown in Figure 1. The device consists of a passive nested MZI, i.e., two MZIs (child MZIs) whose inputs and outputs are combined to form a larger MZI (parent) (Figure 1a). We use 2 × 2 multimode interference (MMI) couplers to form the child MZIs. This configuration provides supplementary inputs and outputs for the characterization of the single child MZI (Figure 1). Each arm of the child MZIs is equipped with a graphene modulator and a thermal phase shifter (TPS), while the parent arms are provided with TPSs at the output of the child MZMs. The photonic platform is a standard 220 nm silicon-on-insulator (SOI) with a silica (SiO$_2$) buried-oxide (BOX) of 3 $\mu$m and a SiO$_2$ top cladding of 1 $\mu$m. The top cladding is designed to be selectively thinned down to a target of 10 nm residual thickness on top of the Si waveguide only in the regions of the graphene modulator. The TPSs consist of metallic heaters fabricated on top of the 1 $\mu$m SiO$_2$ clad waveguide. The TPS is 200 $\mu$m long and 1.5 $\mu$m wide for a target resistance of 2 k$\Omega$. The Si waveguides are 480 nm wide for single mode quasi-TE operation at 1550 nm wavelength, and grating couplers are used for coupling light in and out of the photonic integrated circuit (PIC). The design of the EAM cross section has been carried out by numerical simulations through a finite element method (FEM) commercial software. In this way, we derived the complex effective index of the device as a function of the graphene chemical potential, i.e. the applied voltage, to optimize the device geometry.

Graphene optoelectronics properties have been extensively described and analyzed in previous works,[1−8] and several designs for amplitude and phase modulation in integrated photonic waveguides have been demonstrated.[43] Based on our previous work,[23,44] we designed double SLG capacitor modulators with a length of 100 $\mu$m, suitable for electro-absorption modulation. While typical I/Q modulators rely on phase modulation, we adopted EAMs because of the more compact dimensions and high-speed of operation due to the associated lower capacitance.[20] The graphene modulator geometry is shown in Figure 1c. The double SLG overlapping region, i.e., the capacitor, is 650 nm wide, while the distance between the graphene metal contacts is 1.5 $\mu$m. The expected bandwidth can be estimated assuming a simplified RC model (Figure 1d) whose time constant depends on the double SLG capacitor and resistive contribution arising from the resistance of the graphene leads from the capacitor to the contacts, the metal to graphene contact resistance and the output resistance of the electronic driver, typically 50 $\Omega$. The −3 dB cutoff frequency as a function of the device dimensions is

$$f_{-3\,\text{dB}} = \left[ 2\pi \cdot \frac{\varepsilon_0 \varepsilon_{\text{diel}}}{t_{\text{diel}}} WL \cdot \left( R_{sh} \frac{(d_{\text{m}} - W)}{L} + \frac{R_{\text{c}}}{L} + R_{\text{o}} \right) \right]^{-1}$$

(1)

where $\varepsilon_0$ is the vacuum dielectric constant, $\varepsilon_{\text{diel}}$ the dielectric constant of the capacitor dielectric, $t_{\text{diel}}$ the thickness of the capacitor dielectric, $W$ the capacitor width, $L$ the capacitor length, $R_{sh}$ the graphene sheet resistance of the leads expressed in $\Omega/\square$, $d_{\text{m}}$ the distance between the metal contacts, $R_{\text{c}}$ the graphene to metal contact resistance expressed in $\Omega\mu$m and $R_{\text{o}}$ the driver output resistance. We used $t_{\text{diel}}$ = 20 nm silicon nitride (SiN) dielectric layer with $\varepsilon_{\text{diel}}$ = 5.35 at 10 GHz frequency, extracted from the RF characterization of dedicated test capacitors (see Supporting Information). Assuming $R_{sh}$ = 1000 $\Omega/\square$ and $R_c$ = 500 $\Omega\mu$m, average values previously measured on wafer scale test structures,[11] we estimated $f_{-3\,\text{dB}}$ = 15 GHz.

The passive photonic waveguides and grating couplers were fabricated by e-beam lithography. The metallic heaters are
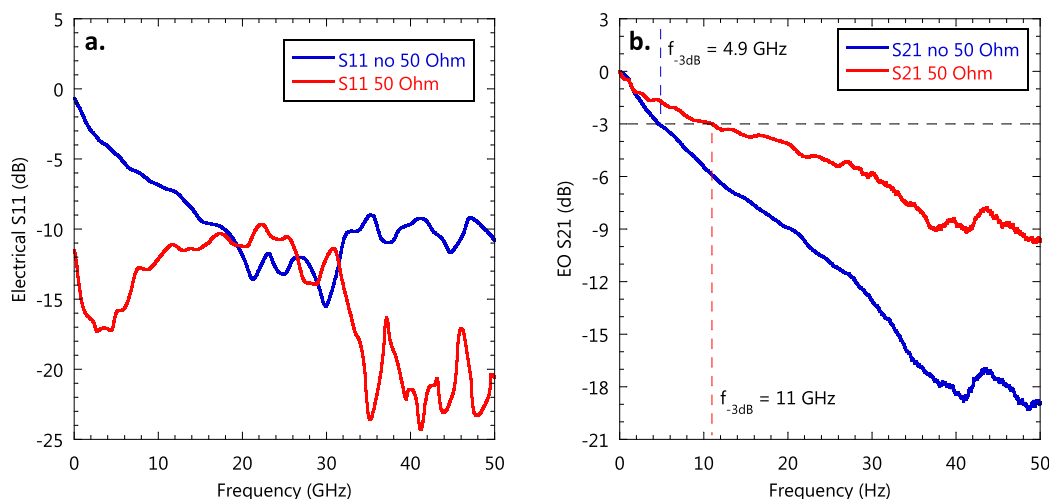
**Figure 3.** (a) Double SLG EAM electrical S11 vs frequency with (red line) and without (blue line) an external 50 Ohm shunt load. (b) Double SLG EAM electro-optical S21 vs frequency with (red line) and without (blue line) an external 50 Ohm shunt load.

made of a 70 nm titanium (Ti) thin film and are routed to the pads for probing by a stack of 70 nm Ti and 150 nm gold (Au). We used commercially available polycrystalline graphene films.[45] We transferred the first SLG on top of the waveguides by a water assisted transfer process[46] and patterned by e-beam lithography and plasma etching (for graphene characterization, see Supporting Information). The first metal contact is obtained by evaporation of a stack of 7 nm nickel (Ni) and 150 nm Au films patterned by e-beam lithography. Single layer, wafer scale, commercial hexagonal boron nitride (hBN) is then transferred with the same transfer process as a protection layer onto the graphene layer. Then the 20 nm ($t_{diel}$) thin film of stoichiometric SiN was deposited by PECVD at 300 °C onto the hBN/SLG stack. Then, the second layer of graphene and its contact are processed in the same way as for the first layer.

## RESULTS AND DISCUSSION

**EAM and TPS Characterization.** Stand-alone graphene EAMs, with the same geometry used in the I/Q MZM, have been also fabricated on the same PIC, to characterize the stand-alone electro-absorption performance. Figure 2 shows the transmissions at 1550 nm wavelength as a function of the applied voltage at the output of two EAMs: the first on the left driven in the high voltage range from −25 to 25 V (Figure 2a), the second in a reduced range between −10 and 12 V (Figure 2b). The curves are normalized to the insertion loss (IL) of the passive waveguide (~10 dB mainly due to the input/output grating couplers, measured by cut-back method on dedicated test structures).

We observed a maximum change of transmission (extinction ratio ER) of 4.8 dB from 6 to 25 V, and a device IL of 8 dB measured at the maximum transparency. The device exhibited a significant charging and hysteretic behavior most likely due to charge trapping at the interface with the SiN. This mechanism is kept under control when the applied voltage is kept below 15 V as shown in Figure 2b. The measured modulation efficiency is 0.75 dB/V in the range of 6−12 V. The curves in Figure 2 are not centered with respect to 0 V, indicating doping of the transferred SLGs, confirmed by the Raman characterization (see Supporting Information). The measured ER is lower than the estimated 13 dB obtained by finite-element method (FEM) simulations (Supporting In-

formation). This has been attributed to a discrepancy between the target $SiO_2$ cladding thickness on top of the waveguide (10 nm) and the fabricated thickness, experimentally estimated to be ~60 nm by fitting of the experimental curves with numerical simulation (Figure 2c). This deviation significantly affects both the ER and the modulation efficiency (Supporting Information). In fact, the interaction between the evanescent tail of the guided optical mode and the graphene capacitor gets weaker and weaker as the $SiO_2$ on the waveguide gets thicker. By improving the planarization process, the maximum ER can be improved almost three times, while modulation efficiency may be improved from the measured 0.75 to 1.9 dB/V (see Supporting Information). The measured device IL is higher than expected from simulations (<1 dB see Supporting Information). This is most likely due to contamination of the waveguide in the thin cladding region close to the modulator.

The EAM optoelectronic bandwidth has been measured through a vector network analyzer (VNA). The device is connected to the first port of the VNA by means of a radiofrequency (RF) cable and an on-chip RF probe. A CW laser source is coupled to the optical input of the EAM. The resulting modulated output light is detected by a high speed (70 GHz bandwidth) photodiode connected to the second port of the VNA. Prior to the measurement, the VNA is calibrated using a standard calibration procedure to account for the cables, RF probe losses, and photodiode RF response up to 50 GHz. The extracted electro-optical (EO) S11 and S21 parameters as a function of the frequency are shown in Figure 3a and b, respectively. To reduce the RF back reflections from the high impedance EAM (lumped capacitor), we shunted the EAM with an external 50 Ω termination, connected to a second RF on-chip probe contacting the modulator. The reduction of reflections is visible in the S11 parameter curve, which is well below −10 dB up to 20 GHz. The EO S21 shows a −3 dB frequency of 11 GHz that is ~36% lower than expected from simulations. The source of this deviation is most probably due to the large contact resistance obtained from the polycrystalline SLG.

The TPS has been characterized in terms of phase shifting efficiency, i.e., the electrical power needed to obtain $\pi$ shift per unit length. We used a test structure consisting of a balanced
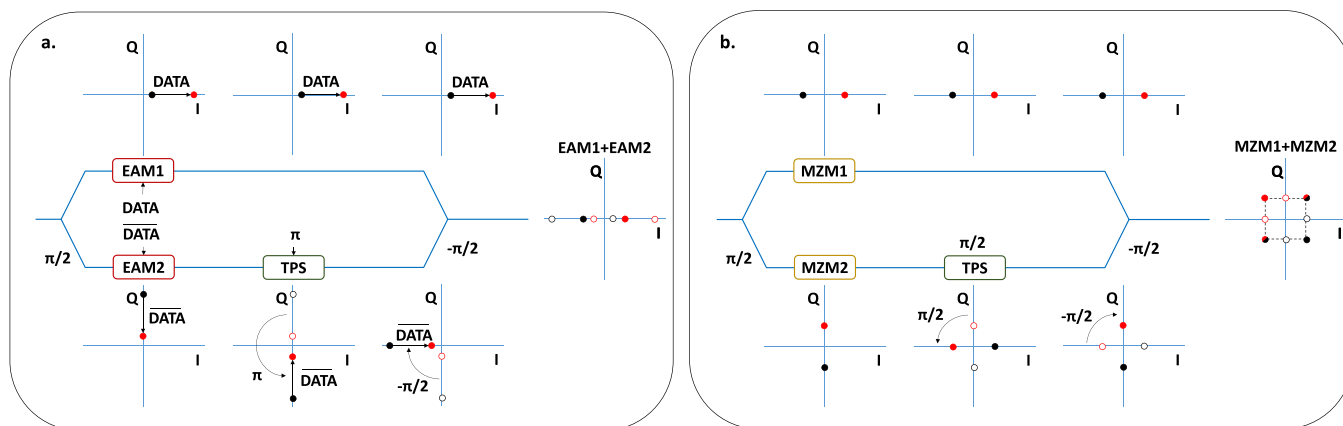
**Figure 4.** (a) Principle of operation of an MZM equipped with differentially driven EAMs and TPSs to obtain BPSK modulation. (b) Principle of operation of an I/Q nested MZM to obtain QPSK modulation. MZM1 and MZM2 are driven according to the scheme of panel a.
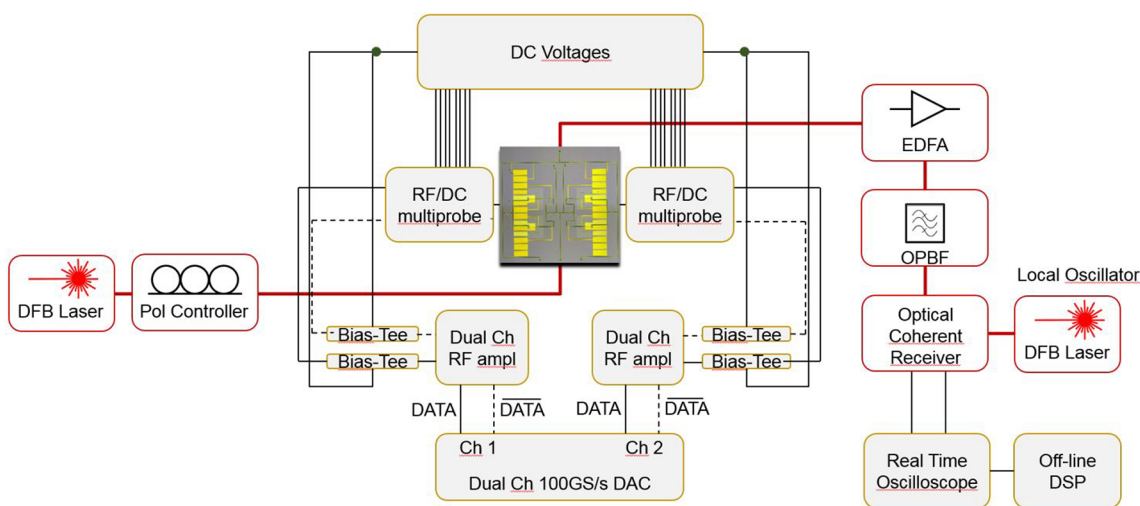


**Figure 5.** Measurement setup for the generation of a QPSK optical signal with the fabricated device. A dual differential channel 100 GS/s DAC is used to generate the binary signals and drive the nested MZM. Reception has been done through an optical coherent receiver connected to a real-time oscilloscope. Off-line DSP was performed to extract the QPSK constellation diagram.

MZI with TPS on both arms and observed the change in the optical transmission of the cross port as a function of the applied electrical power (see plot in the Supporting Information). From the measurements, we extracted a $\pi$ phase shifting efficiency of 4.2 mW mm. On the 200 $\mu$m long TPS device with 2 k$\Omega$ resistance, the driving current (voltage) is 3.2 mA (6.5 V) for $\pi$ shift in the child MZI and 2.3 mA (4.6 V) to obtain $\pi/2$ in the parent MZI.

**I/Q Modulator.** The general principle of operation of I/Q nested MZM for the generation of QPSK and QAM signals lies in the generation of two or multiple levels phase shift keying (PSK) modulation using the child MZMs equipped with PMs and combined together by the parent MZI after introducing a $\pi/2$ phase shift between the two arms.[24] If the PSK is two level (i.e., binary PSK, BPSK), the combined I/Q modulation is QPSK, and for n-PSK, the output is n[2]-QAM. This is typically obtained with PMs and returns carrier-less constellation maps on the I/Q diagram, i.e., centered in the origin.[24] The same result can be obtained with a MZM equipped with EAMs on each arm, which are differentially driven to cancel the carrier and obtain perfectly centered and balanced constellation diagram.[40] The principle of operation is reported in Figure 4.

Figure 4a shows how the BPSK can be obtained with an MZM equipped with two differentially driven EAMs. With reference to the I/Q diagrams, the output of EAM1 is an amplitude modulation on the positive I axis, while the output of EAM2 is an amplitude modulation on the positive Q axis because of the $\pi/2$ introduced by the input 3 dB coupler. The Q signal is then $\pi$ shifted by the TPS and -$\pi/2$ shifted by the output 3 dB coupler, resulting in an amplitude modulation on the negative I axis. After the output 3 dB coupler and assuming EAMs with equal performance, the EAM1 and the EAM2 signals are summed determining two levels perfectly centered with respect to the origin of the I/Q diagram, i.e., a BPSK modulation. This is possible only by differential driving of the EAMs, otherwise the modulation on the two arms would be the same and the MZM output would be a constant value. By implementing the same concept on the second child MZM and adding the $\pi/2$ phase shift, the QPSK is obtained at the output of the nested MZM. This is shown in Figure 4b. If the driving signal is multilevel, the same differential driving scheme allows for square QAM modulation.

We applied the described principle of operation to the graphene nested MZM. The measurement setup is shown on Figure 5.
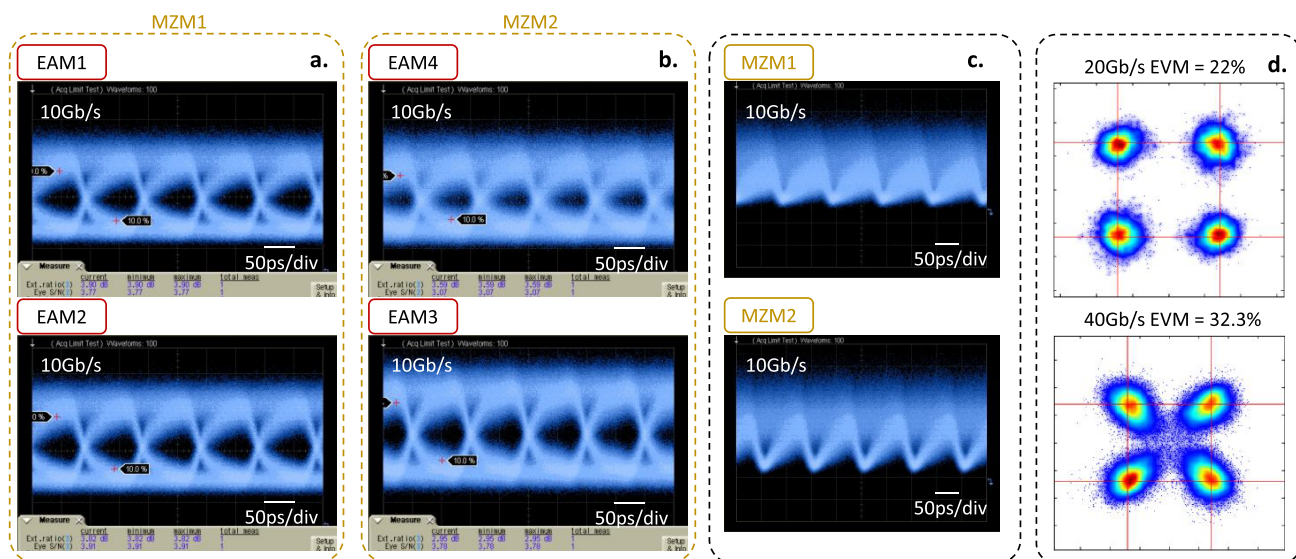
**Figure 6.** (a) 10 Gb/s OOK eye diagrams at the output of the MZM1 when EAM1 is ON and EAM2 is off (top) and when EAM2 is ON and EAM1 is OFF (bottom). (b) 10 Gb/s OOK eye diagrams at the output of the MZM2 when EAM4 is ON and EAM3 is off (top), and when EAM3 is ON and EAM4 is OFF (bottom). (c) 10 Gb/s BPSK eye diagrams at the output of MZM1 (top) and MZM2 (bottom) when EAMs are differentially driven and the TPS is set to the null-point of the MZMs. (d) 20 Gb/s QPSK constellation diagram at the output of the nested MZM.

Because of the high EAMs' IL, the overall IL of the nested MZM is ~30 dB (including input/output coupling losses). For this reason, we used a high-power narrow line width distributed feedback (DFB) laser at the input of the device and a low noise erbium doped fiber amplifier (EDFA) at the output. A fiber polarization controller is used at the input of the device to maximize the light coupling into the PIC. The differential driving signals are provided from a two-channel 100 GS/s digital-to-analog converter (DAC), properly amplified by two >40 GHz dual channel driving amplifiers delivering up to 4.5 $V_{pp}$. We used −6 dB RF attenuator at the output of the amplifiers to reduce the effect of the back-reflections from the capacitive graphene modulators that are not 50 Ω matched.

We first tested the MZMs through the auxiliary optical ports. The graphene EAMs are differentially driven, as previously described. The TPS are tuned to change the output modulation from an OOK ($\varphi \neq \pi$) to a BPSK modulation ($\varphi = \pi$). The eye diagrams are collected by a 70 GHz bandwidth photodetector connected to a sampling oscilloscope. The fabricated TPSs exhibit ~2 kΩ resistance as designed, the electrical power for $\pi$ shift is ~20 mW, corresponding to a $V_\pi \sim 6.5$ V. Figure 6 shows the eye diagrams at 10 Gb/s and the QPSK constellation diagram at 20Gb/s of the fabricated device.

Figure 6a and 6b show the OOK modulation obtained on each of the MZMs when only one of the EAMs is driven (one arm modulating the second not modulating) and measured on the auxiliary output ports. The graphene modulators are biased at 8 V, i.e., where the EAM efficiency is maximized (see Figure 2). The four OOK modulations exhibit similar performance in terms of ER (from 2.95 to 3.9 dB) and S/N (from 3.07 to 3.91). When the two EAMs are differentially driven simultaneously and the TPS is set to 6.5 V (corresponding to $\pi$ shift, i.e., null point of the MZI), the output modulation is a BPSK as shown in Figure 6c. These two signals combined by the parent MZI provide the desired QPSK signal once one of the two is rotated by $\pi/2$ by the parent TPS (Figure 6c). To collect the QPSK signal we used a coherent optical receiver connected to a 20 GS/s real-time oscilloscope. The acquired real-time traces are processed off-line using standard coherent receiver digital signal processing (DSP).[47] Figure 6d shows the collected QPSK constellation diagrams at 20 and 40 Gb/s obtained with the proposed method. The nested MZM exhibit open constellation diagram at 10 Gb/s with estimated EVM of 22% corresponding to a bit-error-rate (BER) of ~3 × 10$^{-6}$.[48] At higher rates, the device was limited by the EAMs bandwidth (11 GHz), but we measured a 40 Gb/s QPSK constellation diagram with estimated 32.3% EVM, corresponding to ~10$^{-3}$ BER. By improving the planarization and transfer process, and by using higher mobility graphene, we expect a significant advancement in terms of modulation efficiency, i.e., at least a factor of 2 as discussed in the previous section. Co-design of the PIC and the driver electronics will be the next to enhance significantly the modulation bandwidth, targeting the baud rates required in the near future, i.e., >100GBaud.

## CONCLUSIONS

In conclusion, we demonstrated for the first time the use of graphene EAMs for the implementation of advanced modulation formats. The double SLG EAMs were fabricated with commercially available polycrystalline graphene and embedded in a nested MZM scheme. We show the characterization of the individual EAMs and child MZMs, and demonstrate the modulation of OOK and BPSK at 10 Gb/s. The I/Q MZM showed QPSK modulation at 20Gb/s with estimated BER ~ 3 × 10$^{-6}$, and at 40Gb/s with estimated BER ~ 10$^{-3}$. This result paves the way to a new set of compact graphene devices for coherent applications potentially operating over an ultrabroad spectrum of wavelengths.

## ASSOCIATED CONTENT

### Ⓢ Supporting Information

The Supporting Information is available free of charge at https://pubs.acs.org/doi/10.1021/acsphotonics.3c00015.

> Methods, additional experimental details, and numerical simulations (PDF)

## ■ AUTHOR INFORMATION

### Corresponding Author

**Vito Sorianello** − *Photonic Networks and Technologies Lab − CNIT, 56124 Pisa, Italy;* ⊙ orcid.org/0000-0003-2204-0778; Email: vito.sorianello@cnit.it

### Authors

**Alberto Montanaro** − *Photonic Networks and Technologies Lab − CNIT, 56124 Pisa, Italy; Tecip Institute − Scuola Superiore Sant'Anna, 56124 Pisa, Italy*

**Marco Angelo Giambra** − *INPHOTEC, CamGraPhIC srl, 56124 Pisa, Italy*

**Nadia Ligato** − *INPHOTEC, CamGraPhIC srl, 56124 Pisa, Italy*

**Wolfgang Templ** − *Nokia Bell Laboratories, 70469 Stuttgart, Germany*

**Paola Galli** − *Nokia Solutions and Networks Italia, 20871 Vimercate, Italy*

**Marco Romagnoli** − *Photonic Networks and Technologies Lab − CNIT, 56124 Pisa, Italy*

Complete contact information is available at:
https://pubs.acs.org/10.1021/acsphotonics.3c00015

### Author Contributions

V.S., M.R., W.T., and P.G. conceived the idea and collaborated to the design of the I/Q modulator and graphene EAMs. M.A.G. and N.L. performed device fabrication. V.S. and A.M. performed the characterization and tests. V.S. wrote the manuscript with the collaboration and contribution of all the authors.

### Notes

The authors declare no competing financial interest.

## ■ REFERENCES

(1) Romagnoli, M.; Sorianello, V.; Midrio, M.; Koppens, F. H. L.; Huyghebaert, C.; Neumaier, D.; Galli, P.; Templ, W.; D'Errico, A.; Ferrari, A. C. Graphene-Based Integrated Photonics for Next-Generation Datacom and Telecom. *Nat. Rev. Mater.* **2018**, *3*, 392−414.

(2) Bonaccorso, F.; Sun, Z.; Hasan, T.; Ferrari, A. C. Graphene Photonics and Optoelectronics. *Nat. Photonics* **2010**, *4*, 611−622.

(3) Castro Neto, A. H.; Guinea, F.; Peres, N. M. R.; Novoselov, K. S.; Geim, A. K. The electronic properties of graphene. *Rev. Mod. Phys.* **2009**, *81*, 109−162.

(4) Wang, F.; Zhang, Y.; Tian, C.; Girit, C.; Zettl, A.; Crommie, M.; Shen, Y. R. Gate-Variable Optical Transitions in Graphene. *Science* **2008**, *320*, 206−209.

(5) Bostwick, A.; Ohta, T.; Seyller, T.; Horn, K.; Rotenberg, E. Quasiparticle dynamics in graphene. *Nat. Phys.* **2007**, *3*, 36−40.

(6) Novoselov, K. S.; Geim, A. K.; Morozov, S. V.; Jiang, D.; Zhang, Y.; Dubonos, S. V.; Grigorieva, I. V.; Firsov, A. A. Electric Field Effect in Atomically Thin Carbon Films. *Science* **2004**, *306*, 666.

(7) Banszerus, L.; Schmitz, M.; Engels, S.; Dauber, J.; Oellers, M.; Haupt, F.; Watanabe, K.; Taniguchi, T.; Beschoten, B.; Stampfer, C. Ultrahigh-Mobility Graphene Devices from Chemical Vapor Deposition on Reusable Copper. *Sci. Adv.* **2015**, *1*, e1500222.

(8) De Fazio, D.; Purdie, D. G.; Ott, A. K.; Braeuninger-Weimer, P.; Khodkov, T.; Goossens, S.; Taniguchi, T.; Watanabe, K.; Livreri, P.; Koppens, F. H. L.; Hofmann, S.; Goykhman, I.; Ferrari, A. C.; Lombardo, A. High-Mobility, Wet-Transferred Graphene Grown by Chemical Vapor Deposition. *ACS Nano* **2019**, *13*, 8926−8935.

(9) Xia, F.; Mueller, T.; Lin, Y. M.; Valdes-Garcia, A.; Avouris, P. Ultrafast graphene photodetector. *Nat. Nanotechnol.* **2009**, *4*, 839−843.

(10) Urich, A.; Unterrainer, K.; Mueller, T. Intrinsic response time of graphene photodetectors. *Nano Lett.* **2011**, *11*, 2804−2808.

(11) Giambra, M. A.; Mišeikis, V.; Pezzini, S.; Marconi, S.; Montanaro, A.; Fabbri, F.; Sorianello, V.; Ferrari, A. C.; Coletti, C.; Romagnoli, M. Wafer-Scale Integration of Graphene-Based Photonic Devices. *ACS Nano* **2021**, *15*, 3171−3187.

(12) Schall, D.; Neumaier, D.; Mohsin, M.; Chmielak, B.; Bolten, J.; Porschatis, C.; Prinzen, A.; Matheisen, C.; Kuebart, W.; Junginger, B.; Templ, W.; Giesecke, A. L.; Kurz, H. 50 GBit/s Photodetectors Based wafer-Scale Graphene for Integrated Silicon Photonic Communication Systems. *ACS Photonics* **2014**, *1* (9), 781−784.

(13) Wang, J.; Xing, Z.; Chen, X.; Cheng, Z.; Li, X.; Liu, T. Recent Progress in Waveguide-Integrated Graphene Photonic Devices for Sensing and Communication Applications. *Front. Phys.* **2020**, *8*, 37.

(14) Nurmohammadi, T.; Abbasian, K.; Mashayekhi, M. Z. Graphene-based tunable plasmon-induced transparency utilizing circular and two rectangular gold rings in the near-infrared spectrum. *Mater. Sci. Semicond.* **2022**, *144*, 106601.

(15) Nurmohammadi, T.; Abbasian, K.; Mashayekhi, M. Z. Tunable modulators based on single and double graphene-based resonator systems in the mid-infrared spectrum. *Optik.* **2022**, *271*, 170195.

(16) Liu, M.; et al. A graphene-based broadband optical modulator. *Nature* **2011**, *474*, 64−67.

(17) Liu, M.; Yin, X.; Zhang, X. Double-layer Graphene optical modulator. *Nano Lett.* **2012**, *12*, 1482−1485.

(18) Koppens, F. H. L.; Mueller, T.; Avouris, P.; Ferrari, A. C.; Vitiello, M. S.; Polini, M. Photodetectors Based on Graphene, Other Two-Dimensional Materials and Hybrid Systems. *Nat. Nanotechnol.* **2014**, *9*, 780−793.

(19) Sorianello, V.; Midrio, M.; Contestabile, G.; Asselberghs, I.; Van Campenhout, J.; Huyghebaert, C.; Goykhman, I.; Ott, A. K.; Ferrari, A. C.; Romagnoli, M. Graphene-Silicon Phase Modulators with Gigahertz Bandwidth. *Nat. Photonics* **2018**, *12*, 40−44.

(20) Giambra, M. A.; Sorianello, V.; Miseikis, V.; Marconi, S.; Montanaro, A.; Galli, P.; Pezzini, S.; Coletti, C.; Romagnoli, M. High-Speed Double Layer Graphene Electro-Absorption Modulator on SOI Waveguide. *Opt. Express* **2019**, *27*, 20145−20155.

(21) Agarwal, H.; Terres, B.; Orsini, L.; Montanaro, A.; Sorianello, V.; Pantouvaki, M.; Watanabe, K.; Taniguchi, T.; Thourhout, D. V.; Romagnoli, M.; Koppens, F. H. L. 2D-3D integration of hexagonal boron nitride and a high-κ dielectric for ultrafast graphene-based electro-absorption modulators. *Nat. Commun.* **2021**, *12*, 1070.

(22) Marconi, S.; Giambra, M. A.; Montanaro, A.; Miseikis, V.; Soresi, S.; Tirelli, S.; Galli, P.; Buchali, F.; Templ, W.; Coletti, C.; Sorianello, V.; Romagnoli, M. Photo thermal effect graphene detector featuring 105 Gbit s−1 NRZ and 120 Gbit s−1 PAM4 direct detection. *Nat. Commun.* **2021**, *12*, 806.

(23) Sorianello, V.; Contestabile, G.; Romagnoli, M. Graphene on Silicon Modulators. *J. Lightwave Technol.* **2020**, *38*, 2782−2789.

(24) Seimetz, M. *High-Order Modulation for Optical Fiber Transmission*; Springer-Verlag: Berlin Heidelberg, 2009.

(25) Bigo, S. Coherent optical long-haul system design. *Optical Fiber Communication Conference 2012*, Los Angeles, CA, March 4−8, 2012; p OTh3A.1. DOI: 10.1364/OFC.2012.OTh3A.1.

(26) Seiler, P. M.; Georgieva, G.; Winzer, G.; et al. Toward coherent O-band data center interconnects. *Front. Optoelectron.* **2021**, *14*, 414−425.

(27) Tomkos, I.; Tolmachev, A.; Agmon, A.; Meltsin, M.; Nikas, T.; Nazarathy, M. Low-Cost/Power Coherent Transceivers for Intra-

Datacenter Interconnections and 5G Fronthaul Links. *2019 21st International Conference on Transparent Optical Networks (ICTON)*, Angers, France, July 9−13, 2019; pp 1−5. DOI: 10.1109/ICTON.2019.8840195.

(28) Xie, C.; Cheng, J. Coherent Optics for Data Center Networks. *IEEE Photonics Society Summer Topicals Meeting Series (SUM)* **2020**, 1−2.

(29) Raybon, G.; Adamiecki, A.; Cho, J.; Jorge, F.; Konczykowska, A.; Riet, M. 180-GBaud all-ETDM single-carrier polarization multiplexed QPSK transmission over 4480 km. *2018 Optical Fiber Communications Conference and Exposition (OFC)*, San Diego, CA, March 11−15, 2018; pp 1−3.

(30) Chen, X.; Chandrasekhar, S.; Winzer, P.; Pupalaikis, P.; Ashiq, I.; Khanna, A.; Steffan, A.; Umbach, A. 180-GBaud nyquist shaped optical QPSK generation based on a 240-GSa/s 100-GHz analog bandwidth DAC. *Asia Communications and Photonics Conference (ACP)* **2016**, 1−3.

(31) Zhou, J.; Zhang, Q. Multiple Tb/s Coherent Optical Transceivers for Short Reach Interconnect. *IEEE J. Sel. Top. Quantum Electron.* **2022**, *28*, 8200814.

(32) Doerr, C.; Chen, L.; Vermeulen, D.; Nielsen, T.; Azemati, S.; Stulz, S.; McBrien, G.; Xu, X.; Mikkelsen, B.; Givehchi, M.; Rasmussen, C.; Park, S. Single-Chip Silicon Photonics 100-Gb/s Coherent Transceiver. *Optical Fiber Communication Conference and Exposition (OFC)*, San Francisco, CA, March 9−13, 2014; p Th5C.1. DOI: 10.1364/OFC.2014.Th5C.1.

(33) Ogiso, Y. et al. Ultra-high bandwidth InP IQ modulator for beyond 100-GBd transmission. *Optical Fiber Communication Conference and Exposition (OFC)*, **2019**, M2F.2.

(34) Xu, M.; Zhu, Y.; Pittala, F.; Tang, J.; He, M.; Ng, W. C.; Wang, J.; Ruan, Z.; Tang, X.; Kuschnerov, M.; Liu, L.; Yu, S.; Zheng, B.; Cai, X. Dual-polarization thin-film lithium niobate in-phase quadrature modulators for terabit-per-second transmission. *Optica* **2022**, *9*, 61−62.

(35) Heni, W.; Fedoryshyn, Y.; Baeuerle, B.; Josten, A.; Hoessbacher, C. B.; Messner, A.; Haffner, C.; Watanabe, T.; Salamin, Y.; Koch, U.; Elder, D. L.; Dalton, L. R.; Leuthold, J. Plasmonic IQ modulators with attojoule per bit electrical energy consumption. *Nat. Commun.* **2019**, *10*, 1694.

(36) Zhalehpour, S.; Lin, J.; Guo, M.; Sepehrian, H.; Zhang, Z. All-silicon IQ modulator for 100 GBaud 32QAM transmissions. *2019 Optical Fiber Communication Conference and Exposition (OFC)* **2019**, p Th4A.5.

(37) Li, S.; Li, N.; He, J.; Zhou, R.; Lu, Z.; Tao, Y. J.; Guo, Y. R.; Wang, Y. Silicon intensity Mach−Zehnder modulator for single lane 100 Gb/s applications. *Photon. Research* **2023**, *6*, 109−116.

(38) Wang, C.et al. 100-GHz low voltage integrated lithium niobate modulators. *Conf. Lasers Electro-Opt. (CLEO)* **2018**, SM3B.4.

(39) Burla, M.; Hoessbacher, C.; Heni, W.; Haffner, C.; Fedoryshyn, Y.; Werner, D.; Watanabe, T.; Massler, H.; Elder, D. L.; Dalton, L. R.; Leuthold, J. 500 GHz plasmonic Mach-Zehnder modulator enabling sub-THz microwave photonics. *APL Photonics* **2019**, *4*, 056106.

(40) Melikyan, A.; Kaneda, N.; Kim, K.; Baeyens, Y.; Dong, P. Differential Drive I/Q Modulator Based on Silicon Photonic Electro-Absorption Modulators. *J. Lightwave Technol.* **2020**, *38*, 2872−2876.

(41) Liu, J.; Beals, M.; Pomerene, A.; et al. Waveguide-integrated, ultralow-energy GeSi electro-absorption modulators. *Nature Photon* **2008**, *2*, 433−437.

(42) Wang, Y.; Li, X.; Jiang, Z.; Tong, L.; Deng, W.; Gao, X.; Huang, X.; Zhou, H.; Yu, Y.; Ye, L.; Xiao, X.; Zhang, X. Ultrahigh-speed graphene-based optical coherent receiver. *Nat. Commun.* **2021**, *12*, 5076.

(43) Liu, J.; Khan, Z. U.; Wang, C.; Zhang, H.; Sarjoghian, S. Review of graphene modulators from the low to the high figure of merits. *J. Phys. D: Appl. Phys.* **2020**, *53*, 233002.

(44) Sorianello, V.; Midrio, M.; Romagnoli, M. Design Optimization of Single and Double Layer Graphene Phase Modulators in SOI. *Opt. Express* **2015**, *23*, 6478.

(45) Graphenea, https://graphenea.com.

(46) Ullah, S.; Yang, X.; Ta, H. Q.; et al. Graphene transfer methods: A review. *Nano Res.* **2021**, *14*, 3756−3772.

(47) Ip, E.; Lau, A. P. T.; Barros, D. J. F.; Kahn, J. M. Coherent detection in optical fiber systems. *Opt. Express* **2008**, *16*, 753−791.

(48) Shafik, R. A.; Rahman, an M. S.; Islam, A. H. M. R. On the extended relationships among EVM, BER and SNR as performance metrics. *4th International Conference on Electrical and Computer Engineering*, Dhaka, Bangladesh, Dec. 19−21, 2006; pp 408−411.